J. Fluid Mech. (2006), *vol.* 554, *pp.* 191–216. © 2006 Cambridge University Press
doi:10.1017/S0022112006009426 Printed in the United Kingdom

Transitional pathway to elastic turbulence in torsional, parallel-plate flow of a polymer solution

By BRUCE A. SCHIAMBERG[1], LAURA T. SHEREDA[1], HUA HU[2] AND RONALD G. LARSON[1]†

[1]Department of Chemical Engineering, University of Michigan, Ann Arbor, MI 48109, USA

[2]Proctor & Gamble, West Chester, OH 45069, USA

(Received 21 July 2005 and in revised form 12 February 2006)

Multiple scenarios have been discovered by which laminar flow undergoes a transition to turbulence in Newtonian fluids. Here we show in non-Newtonian fluids a transition sequence to 'elastic turbulence' due to elasticity from polymers, with negligible inertia. Multiple dynamic states are found linking the base flow to 'elastic turbulence' in the flow between a rotating and stationary disk, including circular and spiral rolls. Also, a surprising progression from apparently 'chaotic' flow to periodic flow and then to 'elastic turbulence' is found. These transitions are found in experiments where either shear stress or shear rate is incrementally increased and then held at fixed values; the modes found following stable base flow are 'stationary ring', 'competing spirals', 'multi-spiral chaotic' and 'spiral bursting' modes, followed then by 'elastic turbulence'. Each mode has a distinct rheological signature, and accompanying imaging of the secondary-flow field (simultaneous with rheological measurement) reveals kinematic structures including stationary and time-dependent rolls. The time-dependent changes in the secondary-flow structure can be related to the time-dependent viscosity in the case of several of the modes. Finally, the effect of polymer concentration on the transitional pathway modes is studied systematically.

1. Introduction

Over the last century, various mechanisms have been proposed to describe the emergence of a multiplicity of modes and fully turbulent flow from initially simple flows, including stochastic or strange attractors and period doubling (Landau & Lifshitz 1995). For inertially driven flow instabilities, the transitional states leading from laminar to turbulent flow in simple Newtonian fluids have been studied in idealized flow geometries such as the Taylor–Couette flow between two concentric cylinders (Swinney & Gollub 1985) and in the torsional parallel-plate flow between two coaxial parallel disks (Shouveiler, Le Gal & Chauve 2001; Cros & Le Gal 2002). For these fluids, in flows with circular streamlines, such as the Taylor–Couette example, the centrifugal force can lead to a succession of bifurcations with increasing flow rate (or Reynolds number Re), producing initially simple cellular rolls, followed by spatially and/or temporally modulated rolls, quasi-periodic flow, and chaotic or turbulent flows (Swinney & Gollub 1985). In the related parallel-plate circular-streamline geometry,

† Author to whom correspondence should be addressed: rlarson@umich.edu

https://doi.org/10.1017/S0022112006009426 Published online by Cambridge University Press

experimental studies show a similar progression, including formation of circular and spiral rolls, and turbulent structures, as well as possible spatiotemporal intermittency (Shouveiler *et al.* 2001; Cros & Le Gal 2002). Here we show experimental observations of a transitional pathway to turbulence, driven by a completely different non-inertial force, namely fluid elasticity. We find that the hitherto unexplored transitional pathway to 'elastic turbulence' shows features analogous to those leading to inertial turbulence, inviting efforts to discover theoretical reasons for these similarities.

It has been known for at least two decades that trace amounts of highly elastic polymer in non-Newtonian viscoelastic solutions (with negligible inertia) can lead to purely elastic flow instabilities (Nguyen & Boger 1979; Larson, Shaqfeh & Muller 1990; Larson 1992; Shaqfeh 1996). Because polymeric fluids are often more viscous than simple Newtonian liquids, inertial instabilities are suppressed, but instabilities and secondary flows can occur in polymeric fluids, even at vanishingly small Re, as a result of nonlinearities associated with the elasticity of the fluid (Nguyen & Boger 1979; Larson *et al.* 1990; Larson 1992; Shaqfeh 1996). The clearest and simplest examples of elastic instabilities occur in the Taylor–Couette flow and the torsional rotating parallel-disk shear flow, of viscous highly elastic fluids, where experiments and theory clearly demonstrate a mechanism by which elastic 'normal stresses' give rise to bifurcations to secondary flows (Phan-Thien 1983; Jackson, Walters & Williams 1984; Magda & Larson 1988; Larson *et al.* 1990; McKinley *et al.* 1991; Byars *et al.* 1994). These 'normal stresses' are produced by polymer molecules stretched along circular streamlines, which squeeze fluid inward, leading to a radial pressure gradient (with pressure highest at the inner cylinder), and producing for example the famous 'rod climbing' effect first explained by Weissenberg (1947). (In inertial flows, an analogous centrifugally-driven pressure drop can occur, with pressure greatest at the outer cylinder.) The magnitude of polymer stretch is controlled by the Weissenberg number:

$$Wi \equiv \dot{\gamma}\lambda \tag{1}$$

where $\dot{\gamma}$ is the shear rate and λ the characteristic polymer relaxation time. The analogy between inertial and elastic secondary flows extends further; at high enough Weissenberg number (though still with negligible inertia) the elastic parallel disk flows can show a highly irregular state with spatial and temporal characteristics similar to those of turbulence (Groisman & Steinberg 2000). What remains unexplored, however, is the sequence of bifurcations in a viscoelastic fluid that transforms simple shearing flow to 'elastic turbulence' at high Wi, and how this new route compares to counterpart transitions, such as the inertial turbulence cascade.

In non-Newtonian polymeric fluids, because polymer molecule extension is dependent on local velocity gradient (Larson 1999), unstable modes (which alter the local velocity gradient relative to base flow) can dramatically change the rheological response of the fluid, such as apparent viscosity and first normal stress difference. In these experiments, both imaging of the secondary-flow kinematic structure and measurement of associated, time-dependent viscosity are performed. Measurements of the time-dependent apparent viscosity provide distinct rheological signatures of the various modes.

2. Prior experimental studies of instabilities in torsional shearing flow

Here we summarize experimental findings on the two limiting cases for the torsional parallel-plate flow: the initial mild regular elastic instabilities (Magda & Larson 1988; McKinley *et al.* 1991; Byars *et al.* 1994) and the highly irregular 'elastic turbulent'

https://doi.org/10.1017/S0022112006009426 Published online by Cambridge University Press

state itself (Groisman & Steinberg 2000, 2004). Then we describe recent observations of inertial instabilities and the transition to turbulence in torsional parallel-plate flow of a Newtonian flow.

2.1. *Onset of elastic instability*

Magda & Larson (1988) showed in an experimental study that the apparent 'anti-thixotropic' (or shear thickening) transitions observed earlier (Jackson *et al.* 1984) were, instead, due to instabilities that occurred at a critical shear rate with an inverse dependence on gap, d, in the torsional parallel-plate flow (Magda & Larson 1988):

$$\dot{\gamma}_c \propto 1/d. \tag{2}$$

The gap range studied was $d/R = 0.024$–0.16 (where R is disk radius) for a 1000 p.p.m. polyisobutylene (PIB) fluid (molecular weight $M_w = 2.7 \times 10^6\,\mathrm{g\,mol^{-1}}$, Oldroyd-B relaxation time of 10 s). Furthermore, the role of molecular weight was examined (in this case using a cone-and-plate geometry), demonstrating that the critical shear rate is dependent on molecular weight, and for the lowest molecular weight solution tested, no instability was observed (test solutions were all 1000 p.p.m. PIB, with molecular weights of 1.3×10^6, 2.7×10^6 and 4×10^6–$6 \times 10^6\,\mathrm{g\,mol^{-1}}$, and Oldroyd-B relaxation times of 2, 10 and 27 s, respectively).

McKinley *et al.* (1991) directly imaged an instability pattern and observed that it included three-dimensional radially stratified and time-dependent secondary flow structures for a 3100 p.p.m. PIB solution ($M_w = 1.8 \times 10^6\,\mathrm{g\,mol^{-1}}$, Oldroyd-B relaxation time of 0.794 s). The instability was found to occur at a critical rotational rate or Deborah number (here Deborah number is defined as $De \equiv \lambda\Omega$, where Ω is the angular velocity), consistent with Magda & Larson's (1988) results (equation (2)). Multiple gap-to-radius ratios were studied, from 0.027 to 0.16, and, in imaging experiments, both axisymmetric and non-axisymmetric modes appeared in the flow; there was evidence for an initial overstable (propagating) axisymmetric mode in an experiment at $d/R = 0.127$. These workers found that multiple shear stress states exist for a given shear rate for the parallel-plate flow transition, in a series of experiments where the shear rate was initially above the critical condition and then reduced to find the shear rate at which the flow is no longer unstable; these results showed hysteresis and were reported for $d/R = 0.14$.

Byars *et al.* (1994) directly imaged and quantified the most dangerous instability mode's wave speed and wave dimensions by analysing a time series of images, for two PIB fluids (3100 p.p.m., $M_w = 1.8 \times 10^6\,\mathrm{g\,mol^{-1}}$, 0.794 s Oldroyd-B relaxation time; and 2000 p.p.m., $M_w = 1.8 \times 10^6\,\mathrm{g\,mol^{-1}}$, 1.24 s Oldroyd-B relaxation time) and two aspect ratios ($d/R = 0.05$ and 0.088). The azimuthal wavenumber m, radial wave number α, and wave speed (defined as the imaginary part of κ divided by α, where κ is a complex variable which contains information about instability growth rate and time dependence) of the normal mode equations used to model the linear stability of the flow were determined for these fluids and aspect ratios; these normal mode equations for velocity and stress perturbations in the torsional parallel-plate geometry are of the form (Byars *et al.* 1994):

$$F(r, \theta, z, t) = f(z) \exp[\mathrm{i}\alpha r + \mathrm{i}m\theta + \kappa t], \quad r = -m/\alpha(\theta + \theta_o). \tag{3}$$

The value for m must be an integer, $\alpha > 0$, m/α is the 'winding number', and r, θ and z are the standard cylindrical coordinates. In experiments where the rotational rate of the shearing plate was gradually increased up to and beyond the critical condition,

https://doi.org/10.1017/S0022112006009426 Published online by Cambridge University Press

Byars *et al.* observed initial overstable secondary-flow modes that were either axisymmetric ($m = 0$) or non-axisymmetric ($m \neq 0$), depending on the fluid rheology and aspect ratio d/R. Additionally, at the same shear rate where the initial mode was observed in the flow, it was observed that the unstable flow (as a function of time) can transition to an aperiodic state. They also showed that the secondary flow field (subsequent to formation of the initial unstable mode) possessed wavelengths shorter than the initial mode's wavelength. Finally, the observed initial secondary flow occurred only in an annular region (beyond a first critical radius and less than a second critical radius); this experimental result was explained by an accompanying linear stability analysis using a constitutive equation that included shear thinning which predicted the disappearance of the instability beyond a second critical radius.

Recent theoretical advances in understanding elastic effects in torsional parallel-disk shear flow include work by Avagliano & Phan-Thien (1996, 1999) on the effects of a finite domain and more realistic rheological models on elastic instabilities (although their work is limited to linear stability and axisymmetric perturbations). Additionally, Olagunju (1994) has studied how capillary, inertial and gravitational forces in the base flow of a torsional parallel-plate flow with a free radial surface, entail weak secondary flow near plate edges, as opposed to purely circumferential flow.

2.2. *Elastic turbulence*

Groisman & Steinberg (2000) showed that many of the principal features of inertial turbulence are present in a highly disordered viscoelastic flow, which they named 'elastic turbulence' (test solution was 80 p.p.m. polyacrylamide, $M_w = 18 \times 10^6$; 3.4 s relaxation time based on oscillatory measurements). Both imaging of secondary flow and Doppler velocimeter measurements in a torsional parallel-plate flow showed a power law decay over about a decade in the flow's wavelength (scaled with the gap) and frequency, respectively. Measurement of solution shear stress values for the 'elastic turbulent' state showed an increase by nearly a factor of 20 (depending on the value of d/R) relative to a hypothetical laminar flow (Groisman & Steinberg 2000). They also showed (2004) that 'elastic turbulence' was accompanied by significant increases in the rates of mass transfer relative to what would be expected from simple diffusion in the corresponding laminar flow.

In the original characterization of the 'elastic turbulent' state by Groisman & Steinberg, the large gap ratio ($d/R = 0.263$ and 0.526) in the torsional parallel-plate flow (where an outer fluid retaining wall is necessary because of the large gap, and R here is the upper plate radius) and polymer solution properties evidently result in a more-or-less direct transition from the base flow to 'elastic turbulence,' although a single mediating structure with the shape of a 'toroidal vortex' is noted (Groisman & Steinberg 2000, 2004).

2.3. *Inertial transition to turbulence*

Finally, we summarize here recent Newtonian-flow experiments by Schouveiler *et al.* (2001) on the inertial transitions leading to turbulence in torsional parallel-plate flow, for a range of aspect ratios d/R as a function of increasing Reynolds number, Re_R (where $Re_R \equiv \Omega R^2/\nu$ and ν is the kinematic viscosity. Here, R refers to the stationary disk radius). In their large-gap experiments ($d/R = 0.0714$–0.1429), the first unstable mode to form from the basic flow is inward-propagating axisymmetric rolls which form near the edge of the flow field, followed at higher Re_R by formation of outward-propagating spiral rolls near the edge of the flow field (with the axisymmetric mode still present in the inner region). In this gap range, further increasing Re_R results in 'wave turbulence.' For the small-gap experiments ($d/R = 0.0071$–0.0179), the first

https://doi.org/10.1017/S0022112006009426 Published online by Cambridge University Press

unstable mode observed consists of spiral rolls which are either inward- or outward-propagating. A further increase in Re_R in this gap range leads to 'solitary waves', which are spiral turbulent structures that are not periodic with respect to space or time; these 'solitary waves' co-exist with and overlie the spiral rolls from the previous mode. Further increase of Re_R for specific values of the aspect ratio within the small-gap range can lead to the formation of 'spots' near the edge of the flow field; these 'spots' spiral inward, 'passing through' the spiral roll and 'solitary wave' structures. Finally, upon still further increase in Re_R, the spiral and 'solitary wave' structures are not observed; rather, 'spots' are the only structure observed (now migrating to radial positions closer to the flow centre) and the flow becomes turbulent in the outer radial region. At intermediate values of the aspect ratio ($d/R = 0.0179$–0.0714), Schouveiler *et al.* observed not only some of the modes seen at the other aspect ratios, but also stationary spiral rolls, which were not seen at the other gap ratios. The test fluid in these experiments was water.

In what follows, we report results of experiments with elastic polymeric fluids at small Reynolds number in the torsional parallel-plate flow with a smaller gap ratio than was used by Groisman & Steinberg, where we find a rich series of flow states connecting the base flow to 'elastic turbulence', each possessing distinct time-dependent rheological signatures.

3. Experimental methods

We study polyacrylamide solutions in torsional parallel-plate shearing flow, visualizing secondary flow-field states and simultaneously measuring solution material properties using a torsional rheometer in a 'stress-controlled mode,' where characteristic shear stress, σ (defined below) is incrementally increased, or in a 'rate-controlled mode', where the shear rate $\dot{\gamma}$ is incrementally increased (as $\dot{\gamma}$ varies linearly with radial position, we report its value at the outer radius R). Secondary flow is imaged by means of light-reflective tracer particles in a custom-designed shearing cell (with transparent bottom fixture) that is fixed to the rheometer base (see figure 1). The fluid is confined by a cup, the bottom of which serves as the plate. The gap ratio d/R was set to $d/R = 0.204$, where d is the gap and R is the radius of the upper plate. In a stress-controlled mode, an increase in apparent viscosity $\eta(\dot{\gamma})$ (or the formation or growth in amplitude of an unstable mode) signals the rheometer to decrease $\dot{\gamma}$ relative to experiments where $\dot{\gamma}$ is the control parameter and large increases in $\eta(\dot{\gamma})$ occur:

$$\sigma(\dot{\gamma}) = \eta(\dot{\gamma})\dot{\gamma}. \tag{4}$$

Our classification of states is based on secondary flow-field imaging, rheological change, and fast fourier transforms (FFTs) of time-dependent rheology. Because features of one mode often persist or reappear in subsequent modes (since transitions between modes are gradual in some cases), we report the dominant flow modes and general trends observed, and first illustrate the modes using a representative experiment of a single fluid. To characterize observations of complex waveform patterns or 'roll cells', the normal mode equations from Byars *et al.* (1994; equation (3)) are used; in describing the different spiral patterns observed in our experiments, we assume α is constant and define $Wn \equiv m/\alpha$. Finally, we note that in our so-called 'controlled σ' experiments, the 'shear stress' we report is really the applied torque, T, converted to units of σ (note that the rheometer actually controls torque). The equation used by our rheometer software to apply a 'shear stress' value is based on

https://doi.org/10.1017/S0022112006009426 Published online by Cambridge University Press

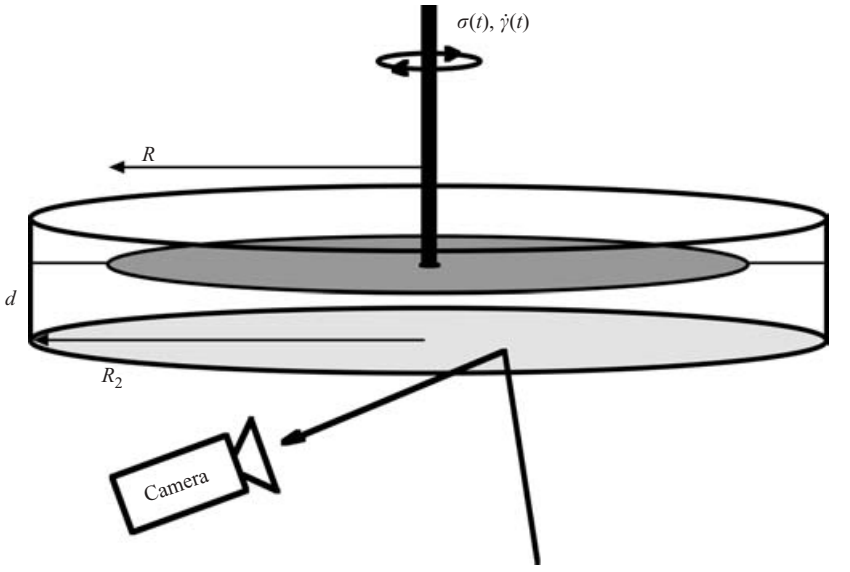


FIGURE 1. Flow-visualization apparatus. The dimensions are $R = 12.5$ mm and $R_2 = 15.5$ mm. The fluid meniscus and free surface are represented by the lines connecting the upper shearing plate to the outer wall. The flow is visualized by seeding test fluid with reflective tracer particle-flakes, which align in the flow direction. Regions of high reflected light intensity correspond to flow in the (r, θ)-plane, and regions of low reflected light intensity correspond to z-direction flow.

the relationship $\sigma = 2T/\pi R^3$ between T and σ (at R) in a Newtonian fluid without secondary flow. Since, in our case, the flow that actually occurs is far from meeting these conditions, σ should not be thought of as an actual shear stress (although we will for simplicity call it 'stress', 'shear stress' or σ throughout this paper), but rather as the torque, expressed in units of stress. In addition, given that our set-up requires a bottom cup, which serves as the bottom plate, there will be additional discrepancy between applied torque and the actual imposed shear stress at a location in the shearing apparatus. Similarly, the 'controlled shear rate' experiments are conducted at a controlled rotation rate of the upper plate, expressed as the shear rate at the rim, for a hypothetical fluid with no secondary flow at the rim (we will refer to this rim shear rate as 'shear rate' or $\dot{\gamma}$ throughout this paper). Finally, we will report an apparent 'viscosity' or η throughout this report which is merely the 'stress' defined above divided by the apparent 'shear rate' at the rim. Of course, when secondary flow is occurring, this 'viscosity' indicates the overall level of viscoelastic stress generated by the flow and is not at all a material property of the fluid.

In the device depicted in figure 1, a mirror was placed at a 45° degree tilt under the bottom glass window, and diffuse illumination was provided using a fibre optic light source, pointed in the direction of (but not directly at) the sample. Reflective tracer seed particles in the test solution are mica/titanium dioxide at 0.1 g/100 ml (Mearlin® Superfine, Engelhard, NJ). The bottom surface of the upper shearing plate was coated with black ink to improve contrast. Plates are aligned parallel within 5 μm over a distance of at least 35 mm, and plates are adjusted to be coaxial using machined semi-cylindrical plastic slabs which fit into the annular region between upper plate edge and inner cylinder wall. The bottom plate is a quartz window, with

https://doi.org/10.1017/S0022112006009426 Published online by Cambridge University Press

anti-reflective coating (Esco Products, Oak Ridge, NJ) with a precision bore glass tube segment affixed (Wilmad Labglass, Buena, NJ). The rheometer is a TA Instruments AR1000. Fluid temperature is monitored before and after each experiment and the solution is allowed to equilibrate for a 20 min (minimum) period before the start of shearing. Stress is incremented in different step sizes, in an attempt to probe states and transitions better.

Flow-field images were recorded in analogue format during experiments lasting around 8 h. For each experiment, images were converted to digital and then greyscale format, and, for the purposes of clarifying illustration, multiple images over a narrow time window (between 0.1 and 0.33 s, depending on the mode) were averaged separately for each mode (this averaging alters slightly 'spiral bursting' and 'elastic turbulent' image patterns, but the images shown here represent the patterns well); then the base flow image was subtracted from the images for all other modes for the particular experiment. After this, the flow-field region was cropped from the larger images. Finally, the contrast and brightness of each image was adjusted to the same degree with reference to each experiment.

4. Fluid characterization and preparation

Our initial test solution is comprised of 492 p.p.m. polyacrylamide of molecular weight $18 \times 10^6\,\mathrm{g\,mol^{-1}}$ (Polysciences, Warrington, PA) dissolved in a viscosified aqueous solution of 65.9 % sugar (sucrose), 0.98 % sodium chloride (NaCl), in water. This polymer concentration is slightly above the overlap concentration, just into the semi-dilute regime. The overlap concentration, c^*, is defined by $c^* \equiv \nu^* M_w / N_A$, where ν^* is the number of polymer molecules per unit volume necessary to yield one polymer molecule, on average, in a fluid volume of R_g^3 (R_g is the polymer radius of gyration), where M_w is the polymer molecular weight, and N_A Avogadro's number. Because excluded volume interactions are of unknown significance, and affect R_g, we here estimate c^* empirically, as the concentration at which addition of polymer roughly doubles the solution viscosity η_0 (where $\eta_0 = \eta_{p,0} + \eta_s$) relative to the solvent viscosity η_s, such that $\eta_0 \sim 2\eta_s$ (Larson 1999).

For our study of the effect of polymer concentration on the transitional pathway (and verification of the transitional pathway using fluids with different rheological properties), polymer test solutions are comprised of 200, 400 and 800 p.p.m. polyacrylamide of molecular weight 5×10^6–$6 \times 10^6\,\mathrm{g\,mol^{-1}}$ (Acros Organics, NJ), also dissolved in a viscous syrup of 65.9 % sugar (sucrose), 0.98 % NaCl, in water. The 400 p.p.m. solution appears to be slightly above the overlap concentration (the borderline between dilute and semi-dilute regimes), based on the empirical estimate described above.

In cone-and-plate experiments, we determined the steady-state relaxation time, λ_{ss}, based on the Oldroyd-B relation $\lambda_{ss} = \Psi_1 / 2\eta_{p,0}$ (Larson *et al.* 1990), for each polymer solution (see table 1). For the 492 p.p.m. fluid ($M_w = 18 \times 10^6\,\mathrm{g\,mol^{-1}}$), λ_{ss} was estimated in this way as 1.0 ± 0.01 s. In figure 2, we show rheometric measurements of the 5–$6 \times 10^6\,\mathrm{g\,mol^{-1}}$ solutions, from which we obtain estimates for $\eta_{p,0}$ and $\Psi_{1,0}$. Based on these measurements, we estimate steady-state relaxation times, λ_{ss}, as 2.3 ± 0.08, 1.5 ± 0.02 and 1.7 ± 0.04 s for the 800, 400 and 200 p.p.m. solutions, respectively. We use λ_{ss} to calculate Wi in this report. In table 1, we summarize the rheological properties of the different fluids (where $\beta \equiv \eta_s / \eta_0$). We encountered some difficulty in observing the zero shear viscosity, η_0, of the $18 \times 10^6\,\mathrm{g\,mol^{-1}}$ fluid, as it had an unusually high viscosity at very low shear rates (either due to instrument sensitivity

https://doi.org/10.1017/S0022112006009426 Published online by Cambridge University Press

	800 p.p.m. polyacrylamide ($M_w = 5$–6×10^6 g mol^{-1})	400 p.p.m. polyacrylamide ($M_w = 5$–6×10^6 g mol^{-1})	200 p.p.m. polyacrylamide ($M_w = 5$–6×10^6 g mol^{-1})	492 p.p.m. polyacrylamide ($M_w = 18 \times 10^6$ g mol^{-1})
η_0 (Pa s)	1.49	0.68	0.43	0.95
$\eta_{p,0}$ (Pa s)	1.24	0.43	0.18	0.70
η_s (Pa s)	0.25	0.25	0.25	0.25
$\beta \equiv \eta_s/\eta_0$	0.17	0.37	0.58	0.26
$\Psi_{1,0}$ (Pa s^2)	5.8 ± 0.19	1.3 ± 0.01	0.6 ± 0.01	1.5 ± 0.02
λ_{ss} (s)	2.3 ± 0.08	1.5 ± 0.02	1.7 ± 0.04	1.0 ± 0.01

TABLE 1. Rheological properties of solutions, at 19 °C.

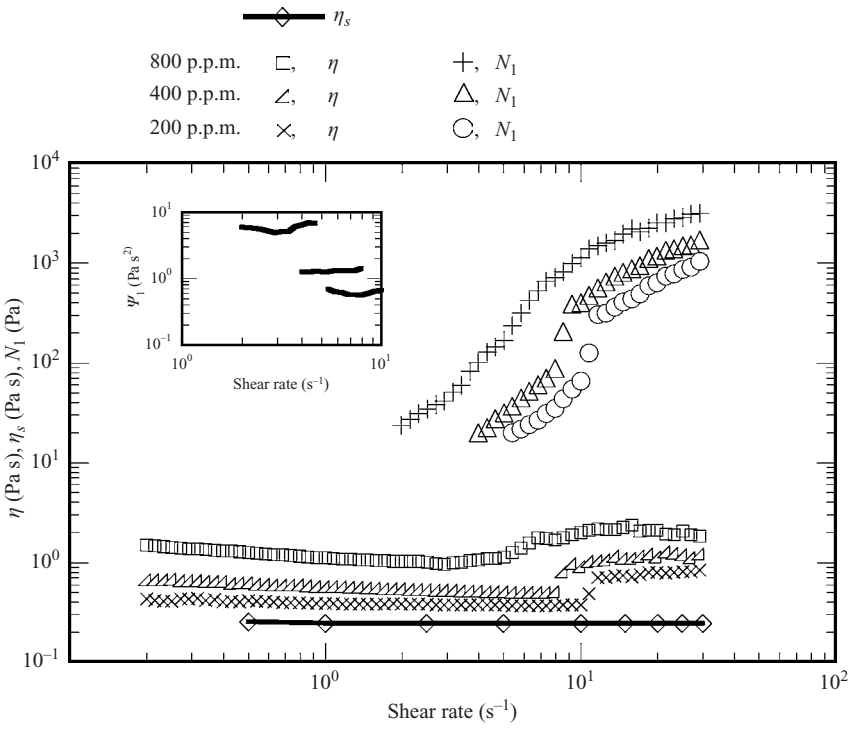


FIGURE 2. Fluid characterization. Plots of η, η_s, and N_1 *vs.* $\dot{\gamma}$ for the 800 p.p.m., 400 p.p.m. and 200 p.p.m. polyacrylamide ($M_w = 5$–6×10^6 g mol^{-1}) solutions. The inset shows plots of Ψ_1 *vs.* $\dot{\gamma}$ for the three fluids. The measurements were performed in using a cone-and-plate fixture at 19°C.

limitations or possible solution gel effects at low shear rates), and estimated η_0 when the viscosity began a rough plateau, starting at around 1.8 s^{-1}. Finally, we add that for a similar polyacrylamide ($M_w = 18 \times 10^6$ g mol^{-1}) fluid (not included in this study), we measured a relaxation time from the decay of N_1 following cessation of shear, finding this relaxation time to be about 4 times the Oldroyd-B relaxation time; this ratio is consistent with what has been observed for other Boger fluids, where the ratio was approximately 2.4 to 3 (Shaqfeh, Muller & Larson 1992).

https://doi.org/10.1017/S0022112006009426 Published online by Cambridge University Press

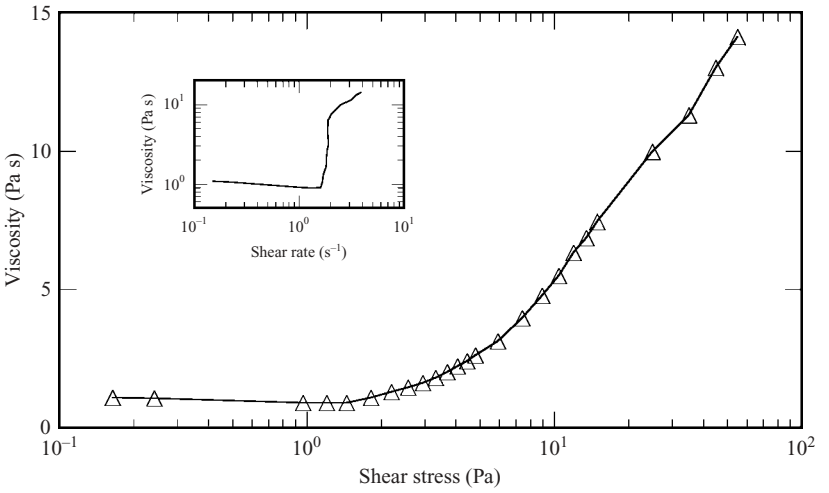


FIGURE 3. Elastic instability progression, general rheological trends for 492 p.p.m. polyacrylamide solution ($M_w = 18 \times 10^6$ g mol^{-1}). Plotted is η_{avg} *vs.* σ over the range 0.16–54.9 Pa, corresponding to $Wi = 0.15$–3.9 and $Re = 0.0014$–0.036. The inset shows a plot of η_{avg} *vs.* $\dot{\gamma}_{avg}$. (Note: to calculate Wi and Re for unstable modes, the average shear rate for the constant stress step is used.)

We note also that in the cone-and-plate measurements shown in figure 2, there is clear evidence of elastic instabilities, as seen in both the apparent shear viscosity and first normal stress coefficient. Rheological measurements of test solutions were performed using a TA Instruments, Rheometric Series, ARES LS rheometer, with all measurements performed at 19 °C using a cone-and-plate fixture (with a radius of 50 mm, and cone angle of 0.04 rad). Solutions are prepared by initially dissolving polyacrylamide in water, prior to dissolution in a concentrated sucrose and water solution, followed by addition of NaCl.

5. Results

5.1. *Identification of a transitional pathway*

Here we focus on secondary flows that develop under slowly increasing controlled stress for a semi-dilute, 492 p.p.m. polyacrylamide ($M_w = 18 \times 10^6$ g mol^{-1}) solution in a viscous Newtonian solvent comprised of 65.9 % sugar (sucrose), 0.98 % NaCl, in water (see figure 3), at room temperature. Similar results were obtained for other solution concentrations, molecular weights and gap ratios, as will be detailed elsewhere. The flow field is visualized over a range of fixed shear stress values, σ, and $\dot{\gamma}$ is measured. (When the experiment is changed from controlled σ to controlled $\dot{\gamma}$, all modes are still seen.) In figure 3, we plot the apparent shear viscosity versus σ, for the range 0.16 to 54.9 Pa, corresponding to $Wi = 0.15$–3.9 and $Re = 0.0014$–0.036. ($Re \equiv \rho V d/\eta_0$, where V is the tangential velocity at R and ρ is the solution density); we observe shear-thickening in the average viscosity (time-average viscosity for each constant shear stress step, typically over a 20 or 10 min period), beginning at $\sigma = 1.4$ Pa (note: there is an expected initial weakly shear-thinning region). The time-dependent shear rates exhibited when each mode is accessed at specific values of σ are shown in figure 4. Figure 4(*a*) represents uniform azimuthal flow or base flow in this geometry. In figure 4(*b*), we show the 'stationary ring' mode, which is an axisymmetric 'ring'

https://doi.org/10.1017/S0022112006009426 Published online by Cambridge University Press

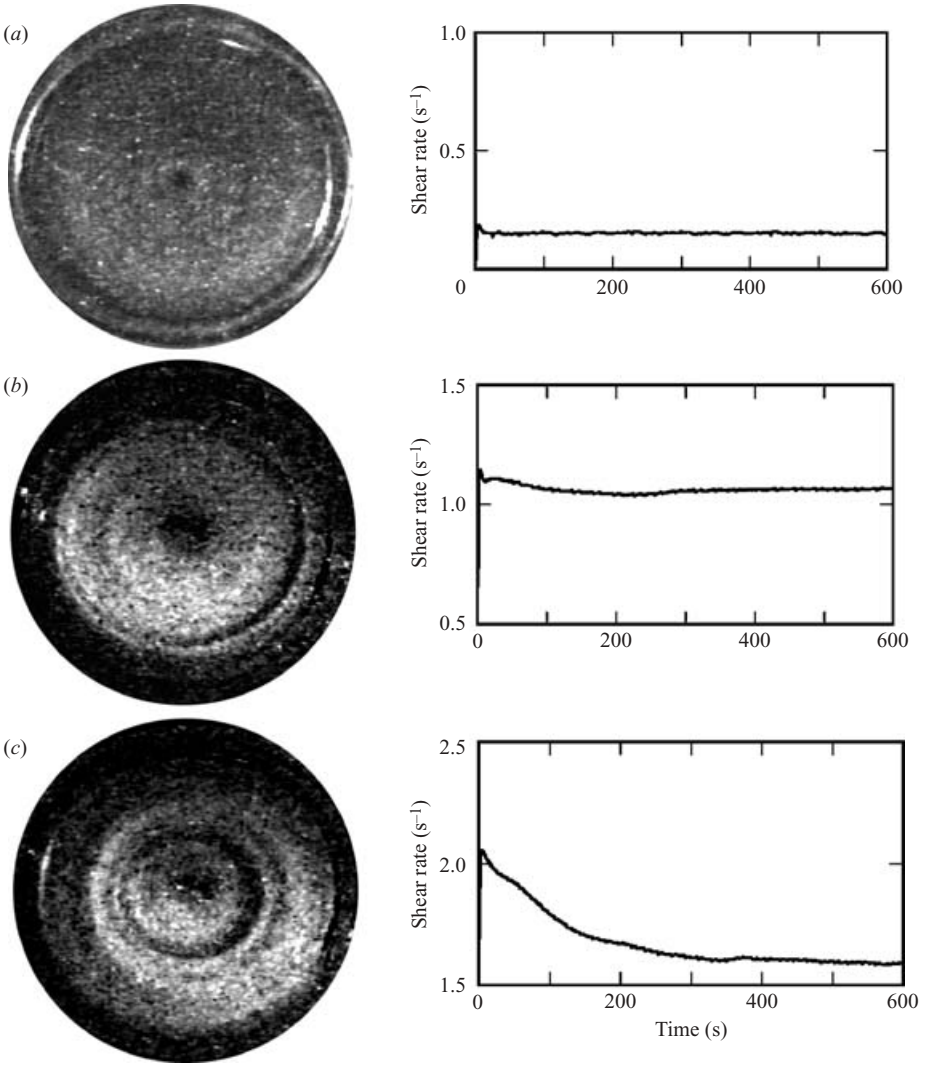


FIGURE 4. Elastic instability progression, initial modes. (*a*) Base state, $\sigma = 0.16$ Pa, $Wi = 0.15$; (*b*) 'stationary ring' mode, $\sigma = 0.96$ Pa, $Wi = 1.1$; (*c*) 'competing spirals' mode, $\sigma = 1.8$ Pa, $Wi = 1.7$ (note: to calculate Wi for unstable modes, the average shear rate for the constant stress step is used).

or set of rings forming in an annular segment of the flow field, accompanied by a shear rate decrease (i.e. an increase in apparent viscosity). The axisymmetric pattern initially forms at approximately the outer edge of the sample and then moves to a progressively smaller radial position as shear stress is increased. Then, in figure 4(*c*), we show the 'competing spirals' mode, which includes formation of an indeterminate pattern of non-axisymmetric spirals and/or axisymmetric rings at the middle to outer radial positions accompanied by a pronounced decrease in shear rate. The inner ring from the 'stationary ring' mode co-exists with the unstable modes in the outer region, but the inner ring moves to progressively smaller radial positions as shear stress is increased. Near the end of the mode (as shear stress is increased), the centre circle begins to blur.

https://doi.org/10.1017/S0022112006009426 Published online by Cambridge University Press

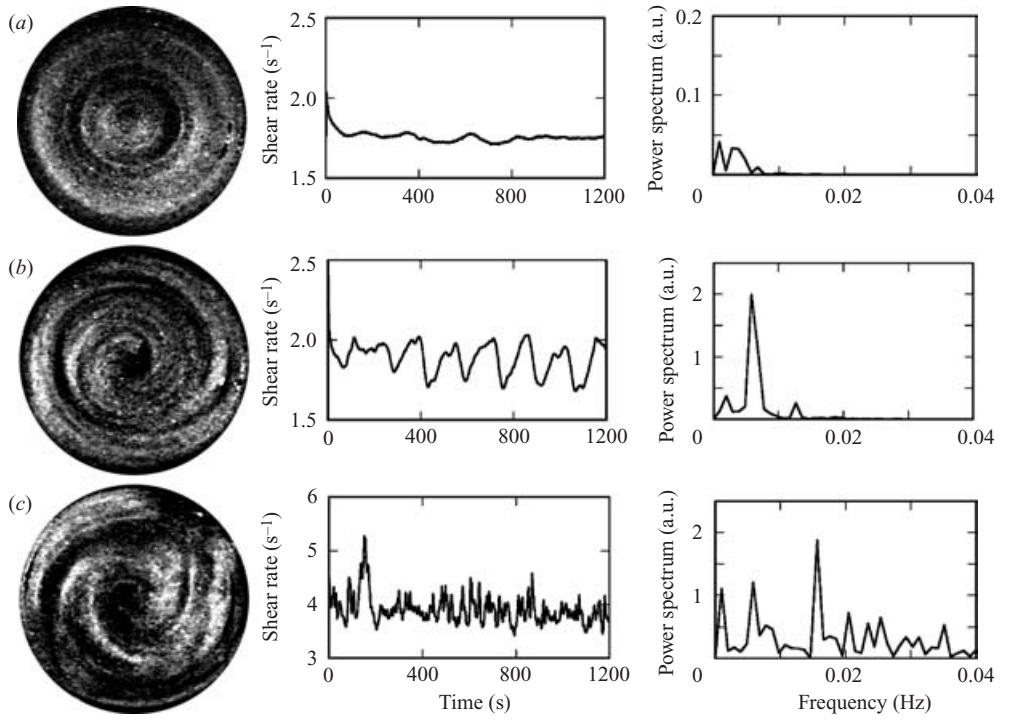


FIGURE 5. Elastic instability progression, final modes. (*a*) 'multi-spiral chaotic' mode, $\sigma = 2.6\,\text{Pa}$, $Wi = 1.8$; (*b*) 'spiral bursting' mode, $\sigma = 7.4\,\text{Pa}$, $Wi = 1.9$; (*c*) 'elastic turbulent' mode, $\sigma = 54.9\,\text{Pa}$, $Wi = 3.9$ (note: the scales on the ordinates of figures 4 and 5 vary). The time period in these steps was 1200 s, with one measurement taken per second. The FFTs are based on the final 1024 data points, to exclude start-up effects. To calculate Wi for unstable modes, the average shear rate for the constant stress step is used. Video sequences of these modes are available as a supplement to the on-line version of this paper.

In figure 5(*a*), we show the 'multi-spiral chaotic' mode, which includes an irregular time-dependent shear viscosity, and formation of spiral modes at all radial locations. At the start of 'multi-spiral chaos', the ring from the competing spirals mode separates from the outer region, and dark thin annular regions form on either side of the ring as the ring grows in amplitude (shown in figure 5*a*). The increased-amplitude ring is then replaced by spirals at the same radial location (not shown). It appears that when the inner ring from the 'competing spirals' mode has decreased in radius and the mode is no longer stable at any radial position, the ring breaks symmetry with respect to the azimuthal coordinate, and a state of 'chaotic' multi-spiral modes ensues. Eventually, at fixed shear stress, the circular ring reforms and stabilizes, and the above sequence is repeated. The pattern-formation cycle is temporally aperiodic, as is reflected in the range of excited low frequencies in $\eta(t)$, revealed by the FFT (see figure 5*a*). The cycle gradually degenerates as shear stress increases, and a transient low winding number (Wn) spiral pattern replaces the 'ring'; and eventually, as stress is increased, the cycle begins to resemble the next mode. In figure 5(*b*), we show the 'spiral bursting' mode, which includes formation of a rapidly propagating spiral of high Wn which begins near the centre of the flow and propagates outward. A lesser Wn and slower-moving spiral then appears and gradually fills in the rest of the flow field, typically accompanied by a maximum in viscosity. The spirals then dampen before

https://doi.org/10.1017/S0022112006009426 Published online by Cambridge University Press

the cycle repeats. The shear rate fluctuations are characterized by growth of a single dominant peak in the power spectrum which corresponds to a 'spiral bursting' cycle.

Finally, we show the 'elastic turbulence' mode in figure 5(*c*). We take the name of this mode from Groisman & Steinberg (2000) who first imaged and named a similar structure with accompanying apparent viscosity increase similar to that in figure 5(*c*) (note: based on the average shear rate in figure 5(*c*), the apparent viscosity increase is about 13 times the base flow viscosity; also see the final data point shown in figure 3). 'Elastic turbulence' is a flow field characterized by very high *Wn* spirals or swirls, periods of loss of alignment of the centre of the secondary flow pattern with the axis ($r = 0$), and occasional and few 'bursts' or returns to the 'spiral bursting' mode. The shear rate fluctuations are characterized by a broad range of excited time-dependent modes, which appear, collectively, aperiodic. The shear viscosity shows a large increase (more than a decade) on entry into the 'elastic turbulent' state. The most convincing evidence that this state deserves the name 'turbulence' lies in the power-law spectrum of velocity fluctuations and in length scales observed, respectively, through laser-Doppler velocimetry and image analysis of mica-flake reflection patterns, carried out by Groisman & Steinberg (2000). We have not replicated these experiments, since thorough characterization of this state to confirm the findings of Groisman & Steinberg is not the purpose of this paper. However, the appearance of the flow, our use of a similar fluid and similar geometry to that of Groisman & Steinberg, and our observation of a similar large increase in stress seen on entry into the flow are all convincing evidence that the flow shown in figure 5(*c*) is indeed the same as that described as 'elastic turbulence' by Groisman & Steinberg. We note that our FFT shows a broad spectrum of modes, which, however, only appears to be a power law if binned more coarsely than done in figure 5(*c*). Velocimetry data, spatial pattern analysis, and extremely long runs (many hours to sample the frequency spectrum thoroughly) would be required for us to check rigorously for power-law temporal and spatial patterns.

5.2. *Effect of polymer concentration*

As an extension of our discovery and characterization of the modes occurring between base flow and 'elastic turbulence' in experiments with the identical polymer and molecular weight (polyacrylamide, $M_w = 18 \times 10^6\,\mathrm{g\,mol^{-1}}$) to that first used by Groisman & Steinberg in their characterization of the elastic turbulent state itself (Groisman & Steinberg 2000, 2004), we performed experiments on new polyacrylamide solutions with different fluid rheology, polymer molecular weight ($5\text{–}6 \times 10^6\,\mathrm{g\,mol^{-1}}$) and concentrations, to explore the generality of the transitional pathway and to test the effects of systematic changes in fluid rheology. In these additional experiments we explored the effect of changing polymer concentration – spanning the dilute to semi-dilute regimes – on features of the various modes comprising this transitional pathway, testing polymer concentrations of 200, 400 and 800 p.p.m. In these experiments, our solvent system was also 65.9 % sugar (sucrose), 0.98 % NaCl, in water, and d/R remained set to 0.204. We confirmed, using these new fluids, that the modes observed in the molecular weight $18 \times 10^6\,\mathrm{g\,mol^{-1}}$ solution can occur in different elastic fluids, and that all previously described modes ('competing spirals', 'multi-spiral chaotic', 'spiral bursting' and 'elastic turbulence') are seen in the new fluids (with few slight differences and exceptions in mode rheological signatures or image patterns, as will be discussed below), at each of the three separate polymer concentrations. In addition, a new periodic mode is stabilized in the most concentrated of the three solutions tested, which we name 'spiral oscillatory' mode.

https://doi.org/10.1017/S0022112006009426 Published online by Cambridge University Press

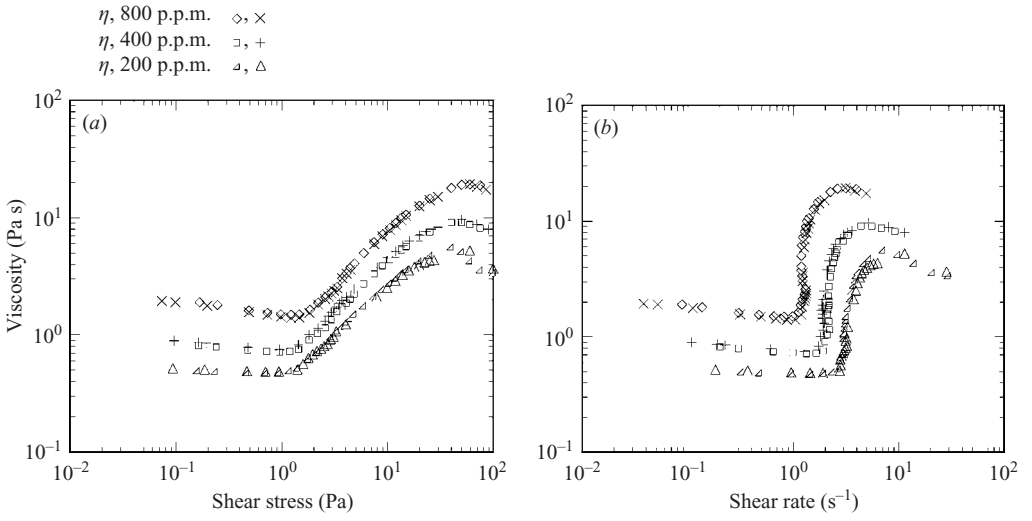


FIGURE 6. Elastic instability progression, general rheological trends as a function of polymer concentration for polyacrylamide with molecular weight $5\text{–}6 \times 10^6$ g mol^{-1}. Each concentration is tested in duplicate experiments and plotted using two different symbols for each concentration. (*a*) Plotted is η_{avg} *vs.* σ; (*b*) η_{avg} *vs.* $\dot{\gamma}_{avg}$ for the same experiments.

In figure 6(*a*), we show shear stress versus apparent viscosity plots for all three solution concentrations tested at $d/R = 0.204$, each in duplicate. In figure 6(*b*), for these same experiments, we show shear rate versus apparent viscosity (where shear rate values are average values for the fixed shear stress holding over the given time interval). The apparent viscosity versus shear stress plots for the three solution concentrations roughly define a single pathway if each data set is adjusted (divided) by a factor of the ratio of zero shear viscosity of the solution to zero shear viscosity of the least concentrated solution (see figure 7). As well, a 'universal' transitional pathway slope is evident in the apparent viscosity versus shear stress plot, for the approximately linear (on a log–log plot), shear-thickening region of the transitional pathway from 1.4 Pa to 22.9 Pa; a linear fit to this region yields a power-law slope of around 0.2 (see figure 7; actual value of the slope is 0.202 ± 0.004). In figure 8, we show images of the secondary flow field for each mode (except 'spiral oscillatory' mode which occurs between 'competing spirals' and 'multi-spiral chaos' in the 800 p.p.m. fluid, and is described below). In figure 9, we show plots of the time-dependent shear rate for each of the modes (excluding 'spiral oscillatory') at all three polymer concentrations. In figure 10, we show FFT plots of the same time-dependent shear rate data, for modes 'multi-spiral chaotic' to 'elastic turbulence'. Note that for the 200 p.p.m. and 400 p.p.m. polyacrylamide fluids, the long-time upward slope of the time-dependent shear rate during 'elastic turbulence' results in large-amplitude low-frequency peaks in the FFT (note: these peaks are off scale in the plots); we believe this long-time upward trend in the time-dependent shear rate (corresponding to a viscosity drop) might be related to possible shear-induced polymer migration, as there is no evidence of fluid degradation (such possible migration has been previously reported in similar viscoelastic fluids (Magda *et al.* 1993)).

An important difference in the responses of fluids tested is that the most concentrated solution (800 p.p.m.) undergoes a periodic oscillatory mode which we name 'spiral oscillatory'. The 'spiral oscillatory' mode bears some similarity to the 'competing

https://doi.org/10.1017/S0022112006009426 Published online by Cambridge University Press

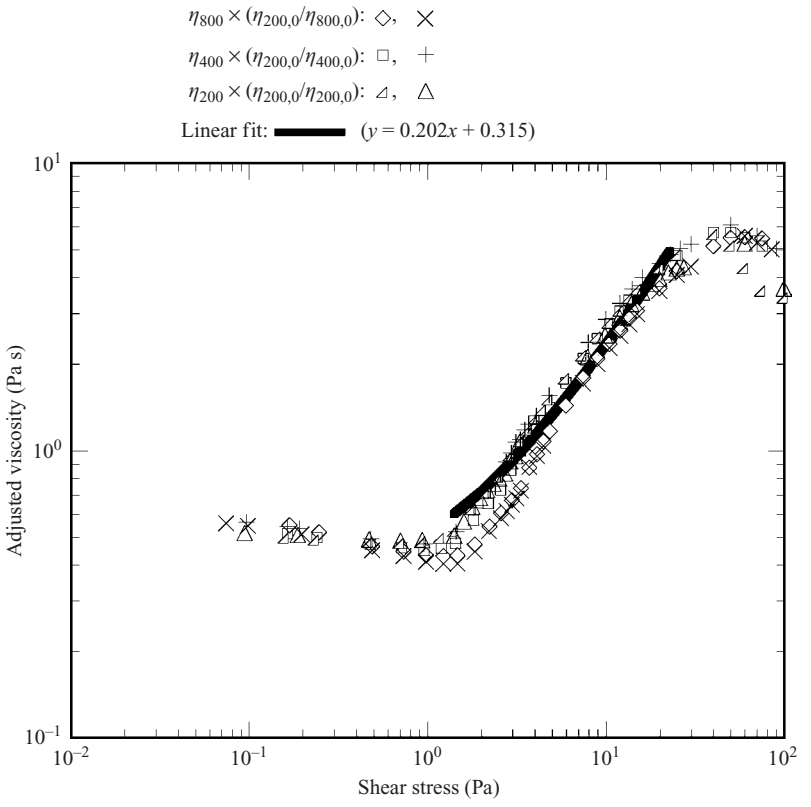


FIGURE 7. Elastic instability progression, a 'universal' transitional pathway slope. Plotted are viscosities for each of the three polyacrylamide ($M_w = 5$–6×10^6 g mol^{-1}) concentrations (800 p.p.m., η_{800}, 400 p.p.m., η_{400}, and 200 p.p.m., η_{200}), from duplicate experiments, where each viscosity has been divided by the ratio of the zero shear viscosity of the solution (which we designate $\eta_{800,0}$, $\eta_{400,0}$ and $\eta_{200,0}$) to the zero shear viscosity of the 200 p.p.m. solution, $\eta_{200,0}$.

spirals' mode, with the important distinction that in the former, the flow field outside the stationary inner ring contains a single (or few) outward-propagating spiral mode(s) that are readily observable. The time-dependent shear rate is clearly periodic, as evident in figure 11. Although only the 800 p.p.m. solutions show the distinct presence of the 'spiral oscillatory' mode (no such mode is distinctly stabilized in the less concentrated 400 and 200 p.p.m. fluids), there is some evidence of the 'spiral oscillatory' mode in these less concentrated solutions. Prior to the 'multi-spiral chaotic' mode, both the 400 and 200 p.p.m. solutions show possible 'spiral oscillatory'-like secondary flow (as determined from video-imaging) and periodicity in the time-dependent shear rate (as determined by FFT), suggesting that the mode may be present, possibly mixed with other competing modes. Also, we have observed in a single experiment for the 400 p.p.m. solution (after the initial onset of 'multi-spiral chaos'), the possible presence of 'spiral oscillatory' features in a hybrid 'spiral oscillatory-multi-spiral chaotic' state, as seen in both the time-dependent secondary-flow image patterns (regular outward-propagating spirals, plus the previously described ring-breaking cycle) and rheological signatures (a strong periodic frequency, plus other low frequencies).

To determine a characteristic wave speed and wavelength of the secondary flow field during the 'spiral oscillatory' mode, we performed image enhancement and analysis

https://doi.org/10.1017/S0022112006009426 Published online by Cambridge University Press

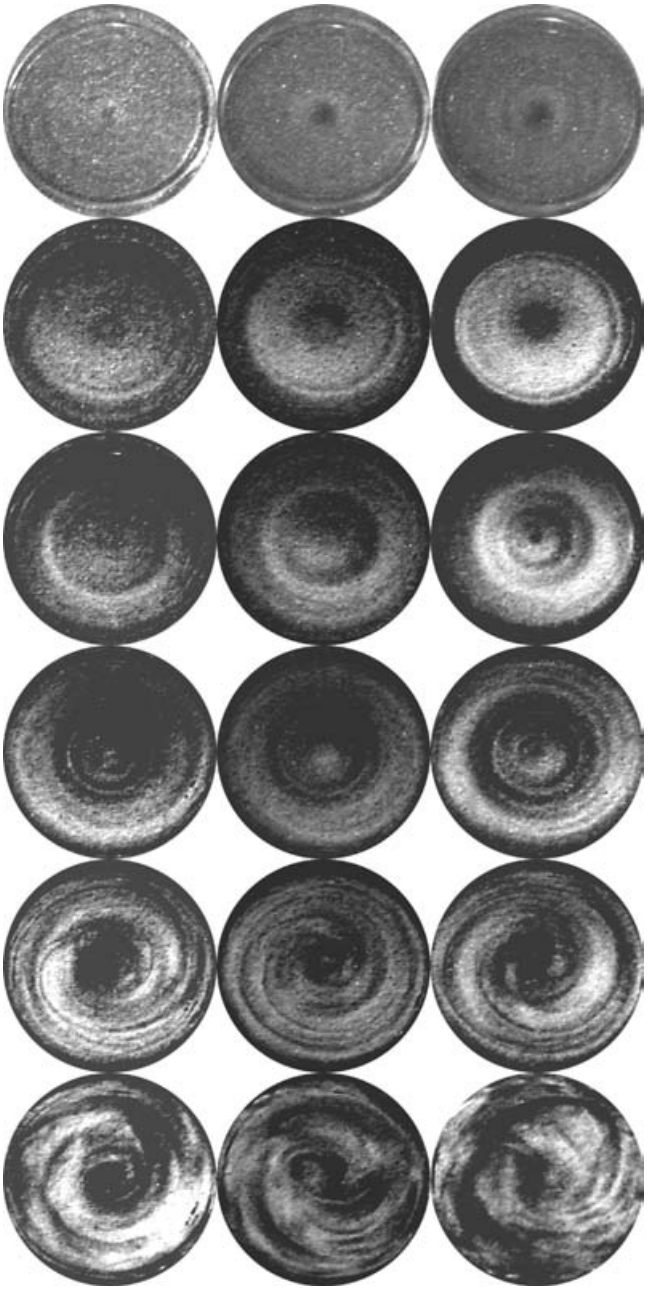


FIGURE 8. Elastic instability progression for various polymer concentrations, secondary flow images. Shown (from left to right) are the 200, 400 and 800 p.p.m. polyacrylamide ($M_w = 5$–6×10^6 g mol^{-1}) fluids. Shown (from top to bottom) are base flow, 'stationary ring', 'competing spirals', 'multi-spiral chaotic', 'spiral bursting' and 'elastic turbulent' modes. Several of the time-dependent modes are most clearly seen in video sequences available as a supplement to the on-line version of the paper (σ and Wi for each of the modes shown above, from top to bottom, for the 200, 400, 800 p.p.m. fluid experiments are, respectively: $\sigma = 0.094$, 0.93, 1.8, 3.1, 13.9 and 59.6 Pa, $Wi = 0.31$, 3.3, 4.7, 5.4, 7.2 and 19.4; $\sigma = 0.096$, 0.96, 1.8, 2.6, 11.9 and 69.7 Pa, $Wi = 0.16$, 1.9, 2.7, 2.9, 3.5 and 11.9; $\sigma = 0.098$, 0.73, 2.2, 3.7, 11.9 and 69.9 Pa, $Wi = 0.12$, 1.1, 2.8, 2.8, 3.2 and 8.8. We note that to calculate Wi for unstable modes, the average shear rate for the constant stress step is used).

https://doi.org/10.1017/S0022112006009426 Published online by Cambridge University Press

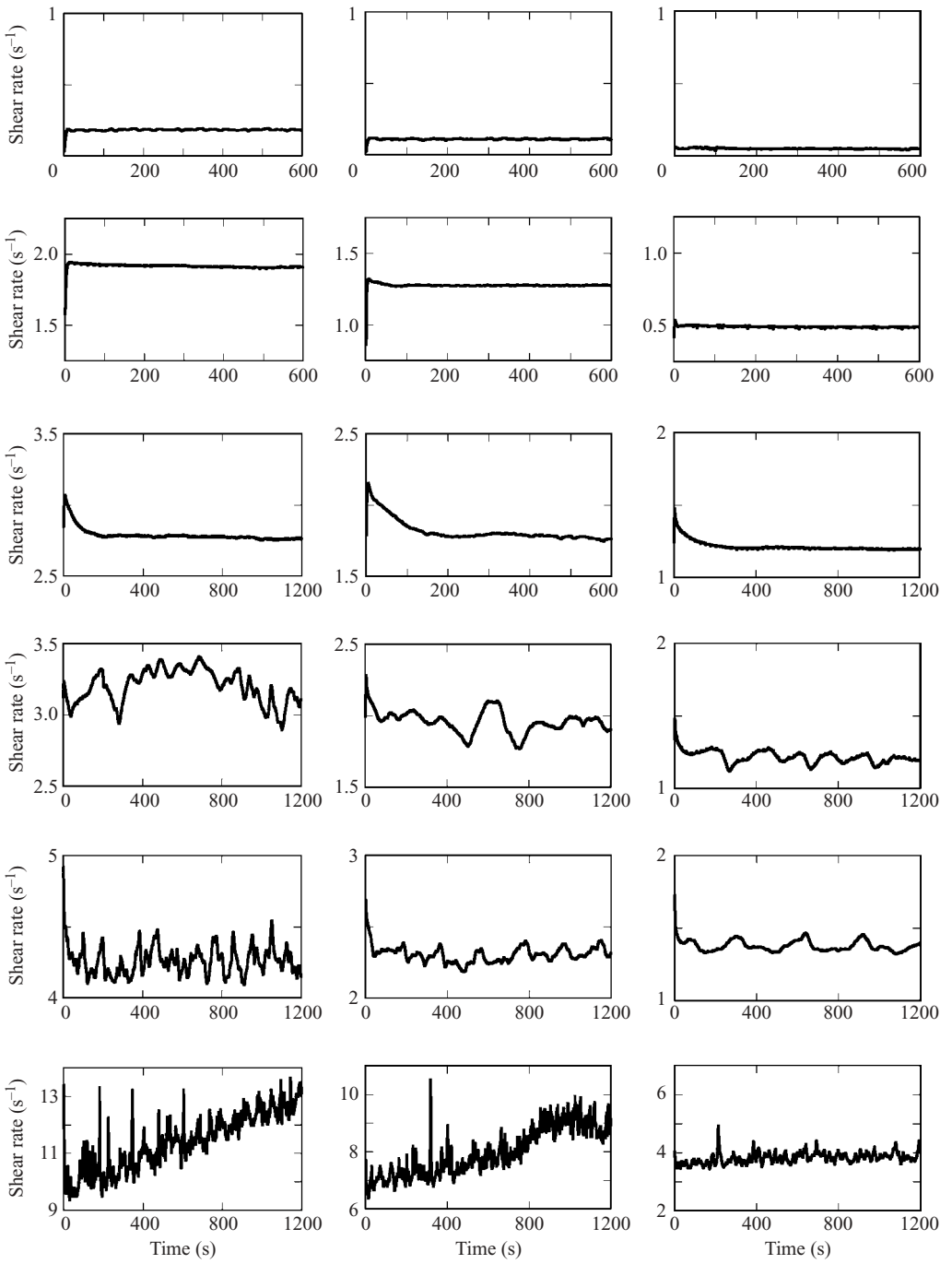


FIGURE 9. Elastic instability progression for various polymer concentrations, rheological signatures. Shown (from left to right) are the 200, 400 and 800 p.p.m. polyacrylamide ($M_w = 5$–6×10^6 g mol^{-1}) fluids. Shown (from top to bottom) are base flow, 'stationary ring', 'competing spirals', 'multi-spiral chaotic', 'spiral bursting' and 'elastic turbulent' modes (σ and Wi for the modes shown above are the same as for the corresponding mode and fluid in figure 8, since data for corresponding fluids are from the same experiments).

https://doi.org/10.1017/S0022112006009426 Published online by Cambridge University Press

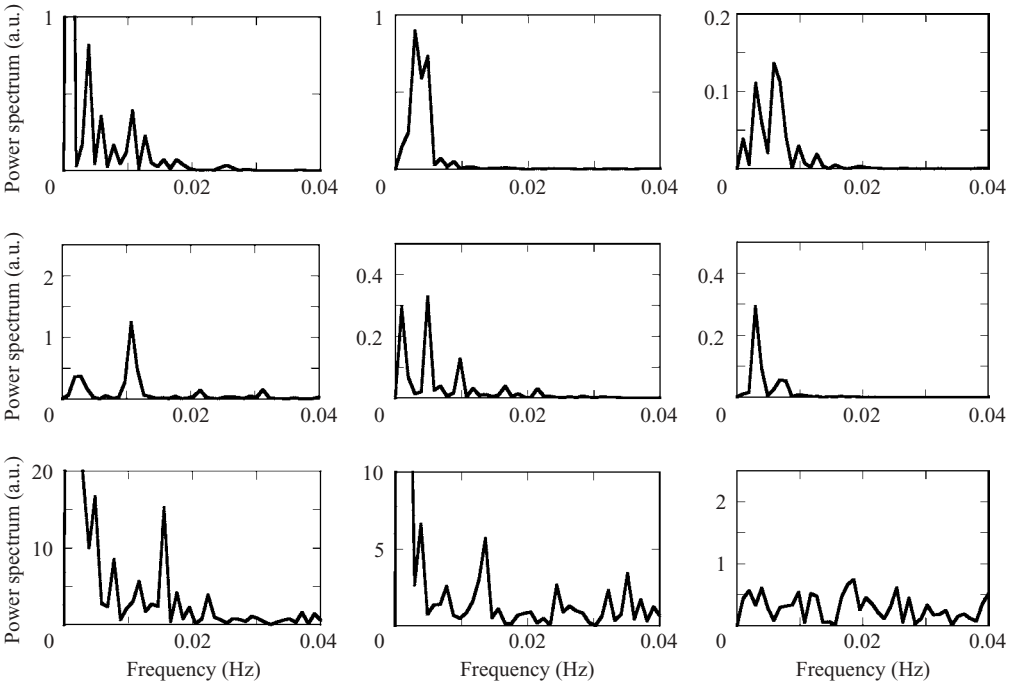


FIGURE 10. Elastic instability progression for various polymer concentrations, FFTs of time-dependent rheological signatures of the 'multi-spiral chaotic', 'spiral bursting' and 'elastic turbulent' modes. Shown (from left to right) are the 200, 400 and 800 p.p.m. polyacrylamide ($M_w = 5\text{–}6 \times 10^6$ g mol^{-1}) fluids. Shown (from top to bottom) are 'multi-spiral chaos', 'spiral bursting' and 'elastic turbulence' (note that for the 'multi-spiral chaotic' mode for the 200 p.p.m. fluid, one of the low-frequency peaks ($f \sim 0.001$ Hz) is off scale, with a value of 4.5. Separately, σ and Wi for the modes shown above are the same as for the corresponding mode and fluid listed in figure 8, since data for corresponding fluids are from the same experiments).

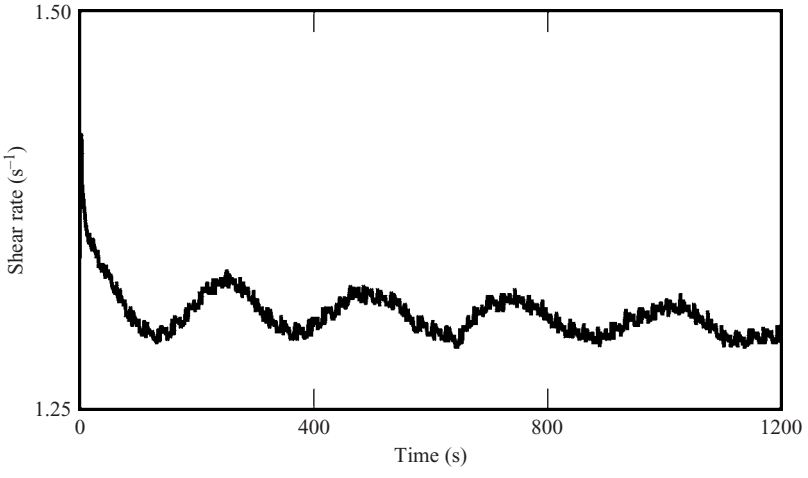


FIGURE 11. Rheological signature of the 'spiral oscillatory' mode. Plot of the time-dependent shear rate for the 800 p.p.m. polyacrylamide ($M_w = 5\text{–}6 \times 10^6$ g mol^{-1}) fluid at $\sigma = 3.0$ Pa.

https://doi.org/10.1017/S0022112006009426 Published online by Cambridge University Press

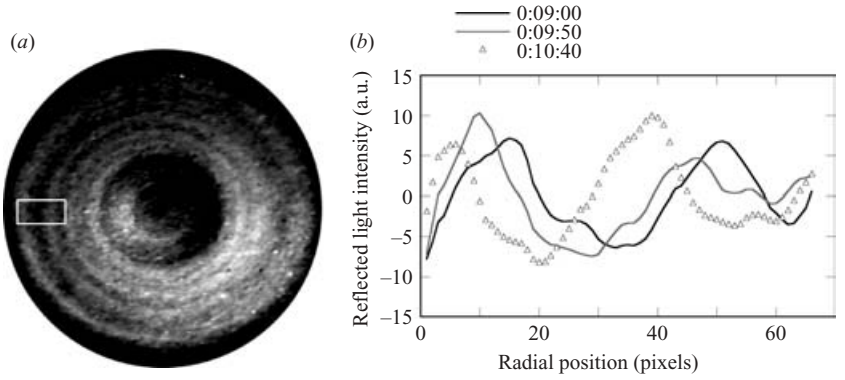


FIGURE 12. Determination of the characteristic wavelength and propagation frequency of the 'spiral oscillatory' mode. (*a*) sample secondary flow-field image and the approximate image region used in the analysis (see boxed region); (*b*) plot of 'image intensity profile' *vs.* radial pixel position (1 pixel = 0.067 mm) average over each of three consecutive 1 s time intervals occurring 50 s apart (see main text for description of image processing, averaging and adjustments used to obtain the 'image intensity profile'). The image shown and data plotted here are from the same experiment and shear stress ($\sigma = 3.0$ Pa) as shown in figure 11, where times in this figure correspond to 9 min, 9 min 50 s and 10 min 40 s after the start of a constant-shear-stress hold at 3.0 Pa. (Note: reflected light intensity is a one-dimensional average of vertical columns of pixel intensity values in the rectangular grid for the box in (*a*), where larger values correspond to brighter regions. Recall that regions of high reflected light intensity correspond to flow in the (r, θ)-plane, and regions of low reflected light intensity correspond to z-direction flow.)

of a flow-field region where the apparent time-dependent propagation of spiral roll cells was readily apparent. The secondary flow-field region was analysed over a 10 min period, based on image sets collected at 50 s intervals. A series of 13 digital image sets consisting of 31 frames (each spaced 1/30 s apart), where the first image in each set occurred, identically, 50 s apart were assembled (a set of 31 images of the base flow was also assembled). The images were converted to black and white, and then each set of 31 images were averaged together to produce a single enhanced image (this was done by averaging corresponding pixels in space over time, separately for each set of 31 images). Subsequently, the base flow was subtracted from each of the enhanced 'spiral oscillatory' mode images. A common set of pixel intensity values corresponding to the region approximated by the rectangle in figure 12(*a*) were used as a basis for estimating the wave speed and wavelength of the mode in the radial direction. Vertical columns of pixel intensity values in the rectangular grid were averaged to produce a single one-dimensional profile for each of the time periods occurring 50 s apart. Separate linear fits to each intensity profile were then subtracted from each of the respective image intensity profiles. In figure 12(*b*), we show three successive, resulting image intensity profiles, where the spiral roll cells are clear (note: at other times during the 10 min period, clear waveforms are not always present and/or two wave peaks are not present in the spatial interval examined). Finally, the one-dimensional profiles for consecutive time period pairs were cross-correlated, and maximum cross-correlation values were used to determine displacements of the propagating 'waves' between image pairs. The average 'wave' displacement between images examined was 6.4 pixels or 0.43 mm, yielding a wave speed in the radial direction of 0.0086 mm s^{-1}. The wavelength was estimated by measuring the pixel distance between maximum intensity values for two wave peaks. As previously noted, in some cases, clear wave peaks or wave pairs are not apparent so data was collected only from images where

https://doi.org/10.1017/S0022112006009426 Published online by Cambridge University Press

two peaks were evident, and an average value was then determined from this set of measurements. The average wavelength was 35.4 pixels or 2.37 mm. The wavelength and wave speed in the radial direction yield a wave period and frequency of 276 s and 0.0036 Hz, respectively; this compares well to the frequency of 0.0039 Hz for the time-dependent shear rate or viscosity, as seen in figure 11 (note: the FFT method for 1024 points bins power into a discretized set of frequencies, including 0.0029, 0.0039 and 0.0049 Hz in the low-frequency range).

The correlation between secondary-flow frequency (as determined by image analysis) and the frequency of the changing shear rate (or apparent solution viscosity) demonstrates that the perturbational mode frequency can be observed in rheometric measurements. This is probably due to the finite dimensions of the shearing apparatus. We believe this is the first demonstration of this correlation, although periodic oscillations (resulting from elastic instabilities) in the apparent viscosity of elastic fluids have been reported elsewhere (Shaqfeh *et al.* 1992). Although the correlation between rheometric measurement and mode frequency becomes considerably more complex as the number of secondary-flow modes in a flow field increases, the connection established here with a single or few modes motivates the argument that the time-dependent viscosity reflects the wavelengths and wave speeds of the unstable flow contained within the shearing apparatus.

We find that the frequency of 'spiral bursting' increases progressively as a function of decreasing polymer concentration. In figure 13, we show FFT results of the time-dependent shear rate during 'spiral bursting' for each concentration, taken from duplicate experiments.

We note here the apparent differences and exceptions in the rheological signatures or image patterns of modes at specific polyacrylamide ($M_w = 5 \times 10^6$–6×10^6 g mol^{-1}) concentrations, compared to the 18×10^6 g mol^{-1} molecular weight polyacrylamide solution experiments. First, the shear rate decrease (or shear viscosity increase) often associated with 'stationary ring' mode secondary-flow pattern can be very slight or not detectable; although there are examples of this for each concentration, we find this is particularly the case for the 200 p.p.m. polyacrylamide fluid (see figure 9). Additionally, although there is a dominant peak in the FFT of the time-dependent shear rate for 'spiral bursting' in the 400 p.p.m. fluid, these experiments also show secondary peaks of the order of 40 to 60 % of the size of the dominant peak (note: the very low-frequency peak at around 0.001 Hz in figures 10 and 13 for a 400 p.p.m. fluid corresponds to a time-dependent viscosity trend occurring over nearly the entire period of 1024 s, which is much slower than the 'spiral bursting' secondary-flow cycle (as seen in video imaging and detected rheologically) that occurs at around 0.005 Hz. This low-frequency large-amplitude peak at around 0.001 Hz is not repeatable, as it did not appear in a separate, identical experiment with a 400 p.p.m. fluid, as shown in figure 13). Finally, in the 'elastic turbulent' mode, the occasional loss of pattern centre with device axis may not always occur (we have in some experiments observed this 'loss of centre', and in other experiments, have either not observed it, or are uncertain if it occurred), although other important features of 'elastic turbulence' are present, including broad disordered spiralling and patterns which closely resemble the images of Groisman & Steinberg (2000, 2004); a dramatic increase in apparent viscosity of approximately 10 times the base flow viscosity for the 800, 400 and 200 p.p.m. solutions; and excitation of a broad spectrum of frequencies as seen in the FFT data. Also, for the 200 p.p.m. fluid in the 'elastic turbulent' mode, although the flow appears turbulent based on image analysis and the broad spectrum of excited time-dependent modes (see figures 8, 9 and 10), something resembling (or actually) 'spiral bursts'

https://doi.org/10.1017/S0022112006009426 Published online by Cambridge University Press

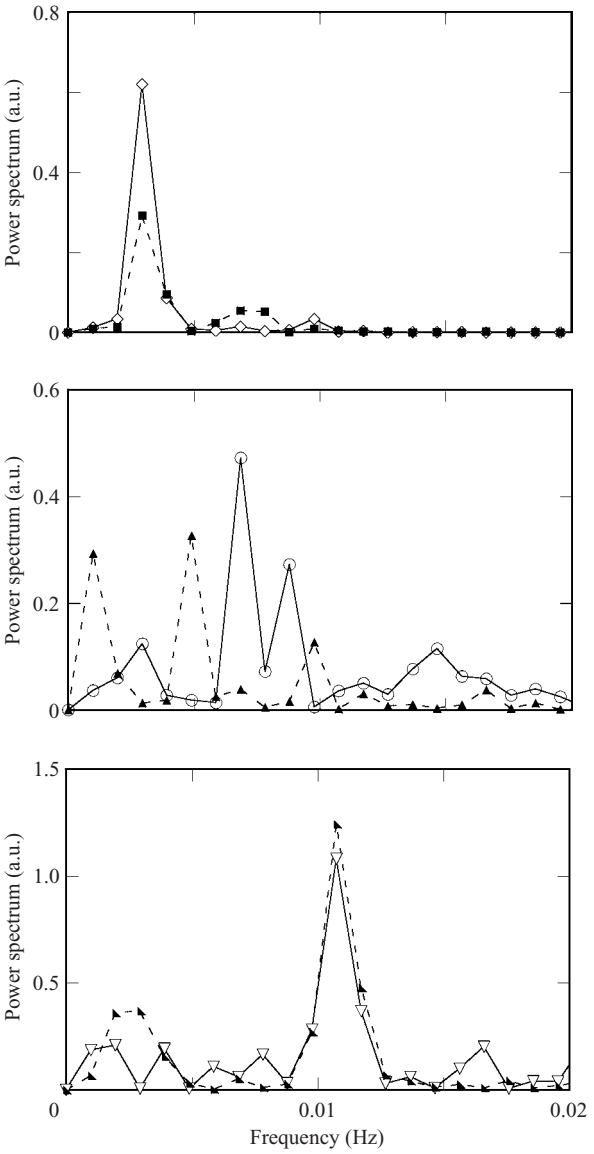


FIGURE 13. 'Spiral bursting' as a function of concentration. Plotted is frequency *vs.* power spectrum, where frequency is an FFT of the time-dependent shear rate at fixed shear stress. Shown (from top to bottom) are the 800, 400 and 200 p.p.m. polyacrylamide ($M_w = 5$–6×10^6 g mol^{-1}) fluids. For each concentration, results from two separate experiments are shown.

persists at approximately 0.014 Hz (as estimated from video imaging analysis), which corresponds to the peak in the FFT of the time-dependent shear rate at around 0.016 Hz (see figure 10). We also recall here that another anomalous feature of the 'elastic turbulent' mode for the 200 and 400 p.p.m. fluids is the marked decline in apparent viscosity (see figure 9); we speculated earlier that this may be due to the possibility of shear-induced polymer migration, as Magda *et al.* (1993) reported the possibility of shear-induced polymer migration in similar viscoelastic fluids. It is unknown what effect the drop in apparent viscosity has on the 'elastic turbulent' mode.

https://doi.org/10.1017/S0022112006009426 Published online by Cambridge University Press

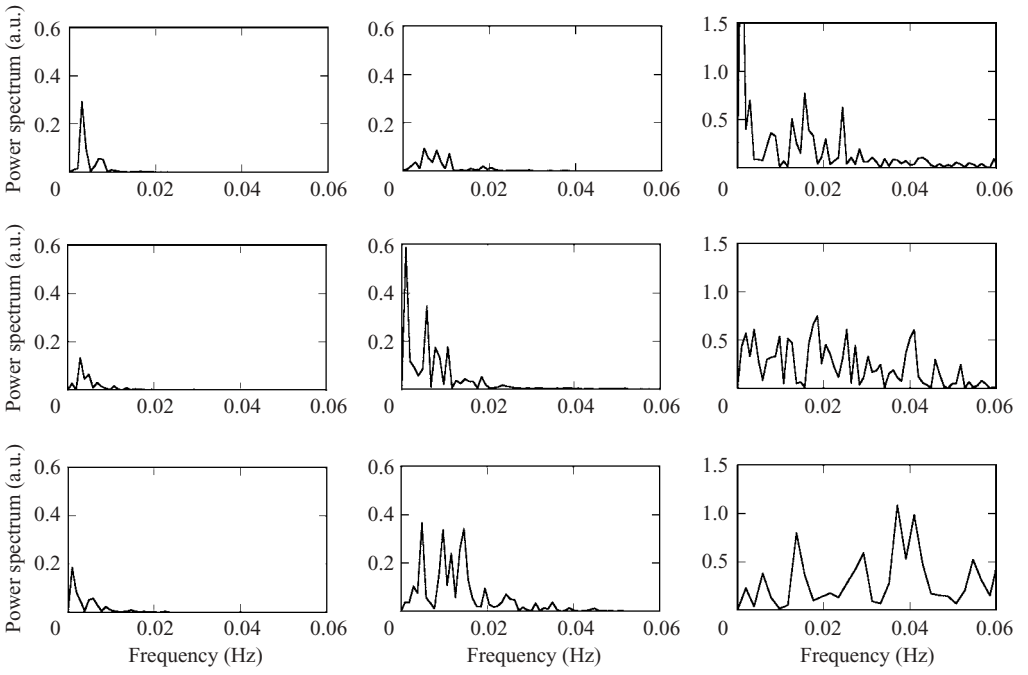


FIGURE 14. Progression from 'spiral bursting' to 'elastic turbulence' – example from a single 800 p.p.m. polyacrylamide ($M_w = 5$–6×10^6 g mol^{-1}) fluid experiment. We show FFTs of the time-dependent shear rate as a function of progressively increasing values of fixed shear stress, from 'spiral bursting' at 11.9 Pa to 'elastic turbulence' at 69.9 Pa and 84.8 Pa. The left-hand column (top to bottom) shows $\sigma = 11.9$ Pa, 13.4 Pa, 14.9 Pa. The middle column (top to bottom) shows $\sigma = 19.9$ Pa, 24.9 Pa, 29.9 Pa. The right-hand column (top to bottom) shows $\sigma = 59.9$ Pa, 69.9 Pa, 84.8 Pa. Note the difference in y-axis scales (0.6 units for 11.9 Pa to 29.9 Pa, and 1.5 units for 59.9 Pa to 84.8 Pa), and note that the very low-frequency point (at approximately 0.001 Hz) for $\sigma = 59.9$ Pa is off scale, with a value of 3.0 units.

5.3. *Additional observations*

Thus far, we have presented evidence for the repeatable occurrence of distinct modes (in multiple fluids) that lead to 'elastic turbulence'. The identified modes represent only part of what is seen in experiments lasting around 8 h. In general, the intermediate states (between modes) appear to be a combination of both the secondary flow structure and rheological signatures of the identified modes occurring before and after these intermediate states. In figure 14, we show FFT of the time-dependent shear rates for the progression from 'spiral bursting' to 'elastic turbulence' that occurred in a single experiment for an 800 p.p.m. fluid at $d/R = 0.204$.

We include here additional observations of the 'stationary ring' mode from experiments using the molecular weight 5–6×10^6 g mol^{-1} polyacrylamide fluids. In experiments with 800 p.p.m. fluids, the 'stationary ring' mode shows a progression from one bright ring to two concentric rings, indicating a likely increase in underlying secondary-flow amplitude and/or roll cell number. We have also observed this progression in a single 400 p.p.m. experiment, but are unable to assess if this multi-ring pattern is present in 200 p.p.m. fluid experiments because the image patterns are too faint.

For the experiments shown in figure 6 using the 5–6×10^6 g mol^{-1} polyacrylamide fluids (each concentration was tested in duplicate), the range of Wi for the 800, 400 and

https://doi.org/10.1017/S0022112006009426 Published online by Cambridge University Press

200 p.p.m. fluids was, respectively (here listed for both experiments): $Wi = 0.20$–9.1, 0.088–11.2; 0.30–13.7, 0.16–16.9; 0.55–49.7, 0.31–48.0. For the same experiments, the maximum Re reached for the 800, 400 and 200 p.p.m. fluids was, respectively (listed here for both experiments): 0.023, 0.028; 0.12, 0.14; 0.59, 0.57 (note: Re numbers reported here for the 200 p.p.m. fluid experiments are for shear stress values around 100 Pa, when the fluid has already undergone or continues to undergo a major decrease in apparent viscosity, which results in a marked rise in shear rate and Re. When the 'elastic turbulent' mode was reached for the 200 p.p.m. fluid shown in figures 8, 9 and 10, at 59.6 Pa, Re was 0.23).

Finally, we have observed on repeated occasions (often after the onset of 'elastic turbulence' and then after the shear stress has been increased to a higher value) that the fluid can detach from part(s) of the cup edge region; all data points (i.e. shear stress steps) where this type of fluid detachment has been observed have been excluded.

6. Discussion

A striking feature of the cascade described above is that after a range of frequencies is excited (see, for example, figure 5*a*), a single, dominant frequency stabilizes in the time-dependent shear viscosity (near 0.006 Hz in this example; see figure 5*b*). Also important to the transition pathway is the evolving cyclical instability in the flow field centre, which appears to connect 'multi-spiral chaos' to 'spiral bursting', leading to 'elastic turbulence', and proceeds from temporal aperiodicity to periodicity and then back to aperiodicity, respectively (note that in the case that 'spiral oscillatory' mode occurs, the progression is from temporal periodicity to aperiodicity, to periodicity, and finally back to aperiodicity). We note additionally that the progression from one secondary-flow mode to the next seems to occur without discontinuous rheological changes for the most part.

The radial structure of the first secondary-flow mode ('stationary ring') is consistent with the results of Byars *et al.* (1994). Furthermore, in our work, as stress increases, the inner ring only remains stable at progressively reduced radial positions (it moves inward), until it is ultimately replaced with spiral non-axisymmetric vortices at all radial positions. Given that the local shear rate and hence the local Weissenberg number increase linearly with radial position in a torsional parallel-plate flow (for stable base-state flow), this suggests that the first instability in this experiment is an axisymmetric mode. Finally, our work resembles recent experiments on Newtonian flows at high Re in the torsional parallel-plate flow which show an analogous progression in symmetry breaking of secondary-flow structures (Schouveiler *et al.* 2001).

We considered the possible unwanted effects of temperature gradients, inertia, and capillary forces on the flow field. Using a thermocouple to measure fluid temperature, we confirmed the absence of viscous heating in these experiments. Examples of measured temperature changes (the temperature before experimentation minus the temperature just after the experiment has ended) for polyacrylamide test solutions (with very similar constituent concentrations to the 492 p.p.m. solution in this report) are $+0.9$, $+0.1$, -0.8 and $-0.6\,^{\circ}\mathrm{C}$, and we believe the fluid temperature closely reflects room temperature. In addition to measuring fluid temperature, we estimated a thermoelastic number for these experiments, $\Theta = Na^{1/2}/De$, where Na is the Nahme–Griffith number ($Na = \eta_0 \chi\, \mathrm{d}^2\dot{\gamma}^2/k\varepsilon$, where $\chi = \varepsilon/\eta_0(|\mathrm{d}\eta/\mathrm{d}\varepsilon|)$, ε is the fluid's temperature in Kelvin units, and k is the fluid's thermal conductivity) and De is the Deborah number for the torsional parallel-plate flow ($De = \lambda\Omega$, where Ω is disk angular

https://doi.org/10.1017/S0022112006009426 Published online by Cambridge University Press

velocity; Rothstein & McKinley 2001). We estimate Θ to be around 0.002 in our experiments, suggesting that elasticity dominates over viscous heating, due in part to the large thermal conductivity of these aqueous solutions (note: in order to approximate $\mathrm{d}\eta/\mathrm{d}\varepsilon$, we used measurements made on an aqueous solvent system with similar sugar concentration to our actual solvent).

A control experiment using only solvent components (with no polymer addition and total solution viscosity comparable to the polymer solution) was performed with $\dot{\gamma}$ as the control parameter, and no patterns or pattern progression were seen like those of the elastic instability modes. We note that at low shear rates, faint diffuse axisymmetric patterns can form (which we believe to be due to colloidal forces), but these disperse rather than intensify as shear rate increases, do not migrate radially, and are less distinct than the axisymmetric patterns of the elastic instability modes. Finally, rheological evidence of all elastic modes was observed in experiments without the imaging-tracer particles, showing that the flow patterns (which have corresponding rheological signatures) were not themselves produced by the presence of the tracer particles.

In order to provide a rough comparison between the stability of the elastic fluids used in our experiments and the various elastic fluids used by previous workers to study elastic instabilities, we compare the critical Deborah numbers ($De \equiv \lambda\Omega$) of our fluids in cone-and-plate experiments (see figure 2) to cone-and-plate data reported by others (for a variety of cone angles and fluid compositions), for the first unstable mode (note that we only present here critical De when an Oldroyd-B relaxation time for the fluid is available). In our experiments, the critical Deborah numbers were approximately 0.3, 0.5 and 0.6 for the 800, 400 and 200 p.p.m. polyacrylamide solutions, respectively (as determined by rheological measurements). These critical Deborah numbers are close to the low end of the range determined by Magda & Larson (1988) (approximately 1 to 9, as determined by rheological measurements, collectively, for the PIB fluids described above), and lower than the critical values determined by McKinley *et al.* (1991, 1995; De of 4.39, as determined by rheological measurements, and De of 4.95 to 7.60, as determined by secondary-flow imaging, respectively. The first set of reported measurements were for the 3100 p.p.m. PIB fluid described above, and the second set of measurements were for the high and low critical values for studies performed on the 3100 and 2000 p.p.m. PIB fluids described above relating to the work of Byars *et al.* 1994). We note that the relationship between polymer concentration and β (in the range studied), and critical shear rate is evident in both the main experiments reported here (see figure 6*b*) as well as in the cone-and-plate measurements of the three fluid concentrations, which also showed instabilities (see figure 2). Our results show that an increase in polymer concentration and therefore in $1-\beta$ correlates to earlier onset of instability as a function of shear rate (as well as shear stress in the case of figure 6*a*). Finally, we note that it was not possible to align all the critical shear rates obtained in our experiments to a single critical condition by either plotting against $\Psi_1\dot{\gamma}/\eta$ or by multiplying the shear rate by the relaxation time (i.e. plotting against Wi); we speculate that this may have something to do with our test solutions spanning the dilute to semi-dilute regimes.

Oscillatory (overstable) modes have been reported previously for purely elastic instabilities, including those in torsional parallel plate flow experiments (Byars *et al.* 1994) and in Taylor–Couette studies (Shaqfeh *et al.* 1992). In the parallel-plate example, the oscillatory modes were detected by flow visualization and quantified by means of image analysis; as an example, the propagation frequency of a mode for the 3100 p.p.m. fluid (described previously) at $d/R = 0.05$ was found to be 1.15 s (the fluid

https://doi.org/10.1017/S0022112006009426 Published online by Cambridge University Press

relaxation time was 0.794 s). In a Taylor–Couette example, an oscillatory mode was detected by rheological measurement (a periodic oscillation in the measured torque, at constant applied shear rate) for a high-molecular-weight polystyrene solution, with a propagation period of approximately 33 s (the fluid relaxation time was 1.27 s, where the relaxation time was an Oldroyd-B relaxation time). Despite the differences in flow geometries and fluids used, we conclude that the time period of 'spiral oscillatory' mode (approximately 260 s, as determined by FFT of the time-dependent torque) is much greater relative to the fluid relaxation time (2.3 s), compared to the examples taken from these two previous studies (Shaqfeh *et al.* 1992; Byars *et al.* 1994).

The shear stress increment protocols used vary from experiment to experiment, but, in general, we attempted to explore multiple shear stress values in regions (of shear stress) where particular modes were expected to form, in experiments lasting around 8 h. The modes we identified often became more distinct over a number of consecutive shear stress steps, and then less distinct over a number of subsequent shear stress steps (signs of subsequent modes also began to appear). For the experiments shown in this report, we have, for the most part, explored the first several modes with 10 min steps (with 1 data point collected per second), and all other modes with 20 min long steps (with 1 data point collected per second). The 20 min (1200 s) holds permitted us to collect enough time-dependent shear rate data for a 1024-point FFT (where the start-up effects could be eliminated by using only the final 1024 measurements to calculate the FFT). The size of the shear stress increments for the experiments shown in this report can be seen in the spacing of the data points in figures 3 and 6(*a*).

For our study with 18×10^6 g mol^{-1} polyacrylamide, we acquired the same material (from the same commercial supplier) as first used by Groisman & Steinberg (2000). In our follow-up experiments, we used a $5\text{–}6 \times 10^6$ g mol^{-1} polyacrylamide material (obtained from a different commercial supplier), and this material behaved more elastically than we would have expected, relative to our 18×10^6 g mol^{-1} polyacrylamide fluid. It turned out that our dilute (200 p.p.m.), borderline (400 p.p.m.) and semi-dilute (800 p.p.m.) concentrations of $5\text{–}6 \times 10^6$ g mol^{-1} polyacrylamide fluids all possess relaxation times greater than our semi-dilute 18×10^6 g mol^{-1} fluid. Also, observed critical shear rates for the $5\text{–}6 \times 10^6$ g mol^{-1} solutions versus the 18×10^6 g mol^{-1} solutions were not in line with what would be expected given the apparent difference in molecular weight. In addition, we did not find our 18×10^6 g mol^{-1} material to be as elastic as Groisman & Steinberg had observed (as indicated by the critical shear rate for onset of elastic instability and turbulence). Therefore, we conclude, that for whatever reason, our 18×10^6 g mol^{-1} polyacrylamide may not be as high in molecular weight as advertised, though we are unable to readily characterize this material by means of gel permeation chromatography. Despite these discrepancies, we emphasize that the modes originally discovered using the 18×10^6 g mol^{-1} polyacrylamide fluid were verified using the $5\text{–}6 \times 10^6$ g mol^{-1} polyacrylamide fluids.

7. Conclusion and suggested future work

In summary, we have mapped a previously unexplored transitional pathway to turbulence, discovering a rich series of secondary flow states connecting simple torsional shearing flow in a parallel plate device to 'elastic turbulence', with negligible inertia. The secondary-flow states involve axisymmetric rolls and non-axisymmetric spirals that compete at high Weissenberg number, producing oscillations, apparent 'chaotic' flow, and, eventually, apparent 'turbulent' flow with a broad spectrum of temporal fluctuations. It is often the case that experimental observations precede and inspire

https://doi.org/10.1017/S0022112006009426 Published online by Cambridge University Press

new theoretical understanding, and these experimental observations provide new insight into the nature of complex transitions and critical phenomena in elastic fluids. Much more is also to be learned from computational fluid mechanics and further experimental studies of the transitions. Eventually, the results can be compared to the transitions leading to turbulence in the corresponding Newtonian flows. In time, we hope that it will be possible to compare experimentally and theoretically the routes to purely elastic turbulence with those for inertial turbulence, leading to a richer understanding of both.

We thank former chemical engineering students J. Baxter, P. Desai and R. Cantor for contributions in the laboratory, and J. Mears for advice and fabrication of parts of the flow-visualization device. We also thank T. A. Instruments' A. Glasman, F. Mazzeo and C. Werzen for their assistance. B.A.S. was supported primarily by a US NIH/CBTP (Grant T32-GM08353) fellowship, and also by a US DOE/GAANN fellowship, under GAANN grant P200A0230-04. Support for other co-authors was provided by NASA, under grant NAG3-2708.

REFERENCES

Avagliano, A. & Phan-Thien, N. 1996 Torsional flow: elastic instability in a finite domain. *J. Fluid Mech.* **312**, 279.

Avagliano, A. & Phan-Thien, N. 1999 Torsional flow stability of highly dilute polymer solutions. *J. Non-Newtonian Fluid Mech.* **84**, 19.

Byars, J. A., Oztekin, A., Brown, R. A. & McKinley, G. H. 1994 Spiral instabilities in the flow of highly elastic fluids between rotating parallel disks. *J. Fluid Mech.* **271**, 173.

Cros, A. & Le Gal, P. 2002 Spatiotemporal intermittency in the torsional Couette flow between a rotating and stationary disk. *Phys. Fluids* **14**, 3755.

Di Prima, R. C. & Swinney, H. L. 1985 In *Hydrodynamic Instabilities and the Transition to Turbulence* (ed. H. L. Swinney & J. P. Gollub). 2nd Edn. Springer.

Groisman, A. & Steinberg, V. 2000 Elastic turbulence in a polymer solution flow. *Nature* **405**, 53.

Groisman, A. & Steinberg, V. 2004 Elastic turbulence in curvilinear flows of polymer solutions. *New J. Phys.* 6, art. 29.

Jackson, K. P., Walters, K. & Williams, R. W. 1984 A rheometrical study of Boger fluids. *J. Non-Newtonian Fluid Mech.* **14**, 173.

Landau, L. D. & Lifshitz, E. M. 1995 *Fluid Mechanics*, 2nd Edn. Butterworth Heinemann.

Larson, R. G. 1992 Instabilities in viscoelastic flows. *Rheol. Acta.* **31**, 213.

Larson, R. G. 1999 *The Structure and Rheology of Complex Fluids*. Oxford University Press.

Larson, R. G., Shaqfeh, E. S. G. & Muller, S. J. 1990 A purely elastic instability in Taylor–Couette flow. *J. Fluid Mech.* **218**, 573.

McKinley, G. H., Byars, J. A., Brown, R. A. & Armstrong, R. C. 1991 Observations on the elastic instability in cone-and-plate and parallel-plate flows of a polyisobutylene Boger fluid. *J. Non-Newtonian Fluid Mech.* **40**, 201.

McKinley, G. H., Oztekin, A., Byars, J. A. & Brown, R. A. 1995 Self-similar spiral instabilities in elastic flows between a cone and a plate. *J. Fluid Mech.* **285**, 123.

Magda, J. J. & Larson, R. G. 1988 A transition occurring in ideal elastic liquids during shear flow. *J. Non-Newtonian Fluid Mech.* **30**, 1.

Magda, J. J., Lee, C. S., Muller, S. J. & Larson, R. G. 1993 Rheology, flow instabilities, and shear-induced diffusion in polystyrene solutions. *Macromolecules* **26**, 1696.

Nguyen, H. & Boger, D. V. 1979 The kinematics and stability of die entry flows. *J. Non-Newtonian Fluid Mech.* **5**, 353.

Olagunju, D. O. 1994 Effect of free surface and inertia on viscoelastic parallel plate flow. *J. Rheol.* **38**, 151.

Phan-Thien, N. 1983 Coaxial-disk flow of an Oldroyd-B fluid: exact solution and stability. *J. Non-Newtonian Fluid Mech.* **13**, 325.

https://doi.org/10.1017/S0022112006009426 Published online by Cambridge University Press

Rothstein, J. P. & McKinley, G. H. 2001 Non-isothermal modification of purely elastic flow instabilities in torsional flows of polymeric fluids. *Phys. Fluids* **13**, 382.

Schouveiler, L., Le Gal, P. & Chauve, M. P. 2001 Instabilities of flow between a rotating and a stationary disk. *J. Fluid Mech.* **443**, 329.

Shaqfeh, E. S. G. 1996 Purely elastic instabilities in viscometric flows. *Annu. Rev. Fluid Mech.* **28**, 129.

Shaqfeh, E. S. G., Muller, S. J. & Larson, R. G. 1992 The effects of gap width and dilute solution properties on the viscoelastic Taylor–Couette instability. *J. Fluid Mech.* **235**, 285.

Swinney, H. L. & Gollub, J. P. 1985 *Hydrodynamic Instabilities and the Transition to Turbulence*, 2nd Edn. Springer.

Weissenberg, K. 1947 A continuum theory of rheological phenomena. *Nature* **159**, 310.

https://doi.org/10.1017/S0022112006009426 Published online by Cambridge University Press